Residual Foveal Cone Structure in *CNGB3*-Associated Achromatopsia

Christopher S. Langlo,[1] Emily J. Patterson,[2] Brian P. Higgins,[2] Phyllis Summerfelt,[2]
Moataz M. Razeen,[2,3] Laura R. Erker,[4] Maria Parker,[4] Frederick T. Collison,[5] Gerald A. Fishman,[5]
Christine N. Kay,[6] Jing Zhang,[6] Richard G. Weleber,[4] Paul Yang,[4] David J. Wilson,[4]
Mark E. Pennesi,[4] Byron L. Lam,[7] John Chiang,[4] Jeffrey D. Chulay,[8] Alfredo Dubra,[1,2,9]
William W. Hauswirth,[10] Joseph Carroll[1,2,9]; for the ACHM-001 Study Group*

[1]Cell Biology, Neurobiology and Anatomy, Medical College of Wisconsin, Milwaukee, Wisconsin, United States
[2]Ophthalmology, Medical College of Wisconsin, Milwaukee, Wisconsin, United States
[3]Alexandria Faculty of Medicine, University of Alexandria, Alexandria, Egypt
[4]Casey Eye Institute, Oregon Health & Science University, Portland, Oregon, United States
[5]Pangere Center for Inherited Retinal Diseases, The Chicago Lighthouse, Chicago, Illinois, United States
[6]Vitreoretinal Associates, Gainesville, Florida, United States
[7]Bascom Palmer Eye Institute, University of Miami, Miami, Florida, United States
[8]Applied Genetics Technologies Corporation (AGTC), Alachua, Florida, United States
[9]Biophysics, Medical College of Wisconsin, Milwaukee, Wisconsin, United States
[10]Ophthalmology, University of Florida, Gainesville, Florida, United States

Correspondence: Joseph Carroll, Department of Ophthalmology, Medical College of Wisconsin, 925 N 87th Street, Milwaukee, WI 53226-0509, USA; jcarroll@mcw.edu.

*See the appendix for the members of the ACHM-001 Study Group.

PURPOSE. Congenital achromatopsia (ACHM) is an autosomal recessive disorder in which cone function is absent or severely reduced. Gene therapy in animal models of ACHM have shown restoration of cone function, though translation of these results to humans relies, in part, on the presence of viable cone photoreceptors at the time of treatment. Here, we characterized residual cone structure in subjects with *CNGB3*-associated ACHM.

METHODS. High-resolution imaging (optical coherence tomography [OCT] and adaptive optics scanning light ophthalmoscopy [AOSLO]) was performed in 51 subjects with *CNGB3*-associated ACHM. Peak cone density and inter-cone spacing at the fovea was measured using split-detection AOSLO. Foveal outer nuclear layer thickness was measured in OCT images, and the integrity of the photoreceptor layer was assessed using a previously published OCT grading scheme.

RESULTS. Analyzable images of the foveal cones were obtained in 26 of 51 subjects, with nystagmus representing the major obstacle to obtaining high-quality images. Peak foveal cone density ranged from 7,273 to 53,554 cones/mm^2, significantly lower than normal (range, 84,733–234,391 cones/mm^2), with the remnant cones being either contiguously or sparsely arranged. Peak cone density was correlated with OCT integrity grade; however, there was overlap of the density ranges between OCT grades.

CONCLUSIONS. The degree of residual foveal cone structure varies greatly among subjects with *CNGB3*-associated ACHM. Such measurements may be useful in estimating the therapeutic potential of a given retina, providing affected individuals and physicians with valuable information to more accurately assess the risk-benefit ratio as they consider enrolling in experimental gene therapy trials. (www.clinicaltrials.gov, NCT01846052.)

Keywords: adaptive optics, cone photoreceptor, fovea, *CNGB3*, achromatopsia, gene therapy

Congenital achromatopsia (ACHM) is an autosomal recessive disorder of cone signal transduction that affects an estimated 1 in 30,000 people worldwide.[1,2] Individuals affected with ACHM experience symptoms including low visual acuity, photo aversion, nystagmus, and impaired or absent chromatic discrimination. Rod-mediated vision in these individuals, however, remains largely normal. Congenital achromatopsia is generally thought to be both structurally and functionally stationary,[3] though there have been reports demonstrating greater photoreceptor disruption in older patients.[4,5] To date, achromatopsia has been associated with a mutation in one of

six genes (*CNGA3*, *CNGB3*, *GNAT2*, *PDE6C*, *PDE6H*, and *ATF6*), with *CNGA3* and *CNGB3* mutations accounting for approximately 70% of all ACHM cases.[3,6–9] Animal models harboring both genetically engineered (mouse) and naturally occurring (mouse, canine, and sheep) mutations in these two genes have been used to demonstrate successful restoration of cone function via adeno-associated virus (AAV)-mediated gene therapy.[10–15] As these therapies are considered for human application,[16] defining the degree of remaining cone photoreceptor structure in patients with ACHM will be important for these efforts to succeed.[17]

Optical coherence tomography (OCT) enables in vivo examination of retinal structure, with the outer hyperreflective bands corresponding to various aspects of the photoreceptor cell.[18,19] A number of investigators have used OCT to examine individuals with ACHM, frequently noting disruption of the ellipsoid zone (EZ) band (also known as the inner segment/outer segment [IS/OS] band) at the fovea.[4,5,16,20–26] The integrity of this band has been shown to range from intact and normally appearing to complete absence, with various levels of disruption in between.[26] However, the lateral resolution of traditional OCT devices does not allow discrimination of individual photoreceptors (namely discrimination of rod versus cone structure), thus OCT provides at best a gross assessment of photoreceptor structure in ACHM.

Adaptive optics scanning light ophthalmoscopy (AOSLO) allows noninvasive imaging of the rod and cone mosaic with cellular resolution.[27–29] With confocal AOSLO, cones in the normal parafoveal retina have a central reflective core and are surrounded by smaller rods, while cones in patients with *CNGA3*- or *CNGB3*-associated ACHM reflect little or no light and appear as dark gaps among the rod mosaic.[20,21,23,25,30] The lack of reflectivity in these cones is suggestive of severely impaired waveguide properties, which is likely a result of some degree of disruption in cone OS structure.[30,31] These cones, which will be referred to as 'remnant' cones, have structural disruption significant enough to impair observation with confocal AOSLO, but nevertheless remain as presumably living cells in the photoreceptor layers of the retina. This disruption to imaging represents a confounder when analyzing confocal AOSLO imagery, in that it is not possible to distinguish between a remnant cone with impaired waveguiding and a gap in the mosaic caused by an absent cone. In contrast, nonconfocal split-detector AOSLO allows observation of cone IS structure in a manner that is thought to be independent of waveguiding—that is, split detector imaging reveals the IS without the need to infer cone locations from gaps in the rod mosaic.[30] This technique has recently been used to elucidate the degree of remnant cone structure in patients with a number of retinal degenerations,[32,33] including four patients with *CNGA3*- and *CNGB3*-associated ACHM.[30]

Despite the evidence for residual cone structure in patients with ACHM, there has been no systematic examination of the variability of remaining cone populations in these patients. To that end, we have undertaken a multicenter natural history study of patients with ACHM caused by mutations in *CNGB3*. Here, we report initial results on residual foveal cone structure in 51 genetically confirmed patients, including findings from OCT, confocal AOSLO, and split-detection AOSLO. We describe the intersubject variability in the density and distribution of remnant foveal cone IS. We likewise describe the variation in OCT phenotype and examine the correlation between OCT and AOSLO findings. As cones are themselves the target for emerging AAV-mediated gene therapy, the degree of residual cone structure, as measured by the number of remnant cones observed with split-detector AOSLO, may serve as a predictor of therapeutic potential across individuals.

METHODS

Subjects

This research followed the tenets of the Declaration of Helsinki and was approved by the institutional review boards at the Medical College of Wisconsin (Milwaukee, WI, USA), Oregon Health & Science University (OHSU; Portland, OR, USA), University of Florida (Gainesville, FL, USA), University of Miami (Miami, FL, USA), and Western Institutional Review Board.

Fifty-one subjects were recruited through one of four sites (Bascom Palmer Eye Institute, Miami, FL, USA; OHSU Casey Eye Institute; The Chicago Lighthouse, Chicago, IL, USA; Vitreo Retinal Associates, Gainesville, FL, USA) where a clinical exam and Early Treatment Diabetic Retinopathy Study (ETDRS) visual acuity assessment were performed. Subjects travelled to the Medical College of Wisconsin for imaging (both eyes of each subject were imaged), where axial length measurements (IOL Master; Carl Zeiss Meditec, Dublin, CA, USA) were obtained for each eye and used to correct the lateral scaling of the retinal images described below. All statistical analyses were conducted using SAS (Cary, NC, USA).

Genetic Analysis

In 48 of 51 subjects, genetic testing was performed by the Molecular Diagnostics Laboratory at the OHSU Casey Eye Institute (Portland, OR, USA) to confirm the presence of mutations in both copies of the *CNGB3* gene (Table). The *CNGA3*, *GNAT2*, *PDE6C*, and *PDE6H* genes were also examined for the presence of mutations (Supplementary Table S1). For the three remaining subjects, genetic testing of *CNGB3* was performed elsewhere—CEI-015 at University of Colorado (Denver, CO, USA), CEI-016 at Children's Hospital of Philadelphia (Philadelphia, PA, USA), and PCI-019 at the Wynn Institute for Vision Research Carver Laboratory (Iowa City, IA, USA).

Optical Coherence Tomography (OCT)

Prior to imaging, one drop each of tropicamide (1%) and of phenylephrine hydrochloride (2.5%) was instilled in each eye for pupillary dilation and cycloplegia. Multiple scans were acquired in each eye of all subjects using the Bioptigen spectral-domain (SD) OCT (Bioptigen, Research Triangle Park, NC, USA). Vertical and horizontal line scans centered on the fovea were obtained, with a nominal scan length of 7 mm (1000 A-scans/B-scan, 120 B-scans). From these, between 10 and 50 B-scans were registered and averaged to improve signal-to-noise ratio using ImageJ software (http://imagej.nih.gov/ij/; provided in the public domain by the National Institutes of Health, Bethesda, MD, USA).[34,35] To ensure the foveal location of these line scans, horizontal and vertical volume scans (nominally 7 × 7 mm) were also obtained (750 A-scans/B-scan, 250 B-scans), and manually inspected to identify the location of the center of the foveal pit. Layer nomenclature follows that of Staurenghi et al.[36] Foveal line scans were graded by two observers (CSL, JC) based on the scheme defined by Sundaram et al.,[26] which specifies the integrity of the EZ (IS/OS) band. Grade I corresponds to an intact band, grade II corresponds to some disruption of the band, grade III corresponds to an absence of the band, grade IV describes a hyporeflective region below the external limiting membrane (ELM), and grade V corresponds to outer retinal atrophy (Fig. 1). Grading was confirmed by examining OCT scans acquired at the individual recruitment sites, which were obtained using the Spectralis SD-OCT system (Heidelberg Engineering, Inc., Heidelberg, Germany). This was done in consultation with an additional observer (MP), and any grading discrepancies were resolved by consensus. The five grading discrepancies that did occur were often due to the position of the scans obtained at the recruitment sites not being centered on the fovea. Outer nuclear layer (ONL) thickness was measured by taking 5-pixel wide longitudinal reflectivity profiles at the foveal center. As in previous studies,[24,26,37–41] the ONL thickness was defined as the distance between the ELM and the next vitread hyperreflective band (Fig. 2). In individuals with complete displacement of the inner retinal layers at the fovea, the vitread

TABLE. Genotype and Retinal Phenotype Summary

Subject	Sex	Age, y	Eye	Genotype	OCT Grade‡	ONL Thickness, μm	Peak Cone Density, Cones/mm²	Visual Acuity Letter Score
BPE-003	F	16	OD	c.1148delC:p.Thr383Ilefs; c.1255G>T:p.Glu419Ter	4	87.36	9,917	8
BPE-010	M	13	OD	c.1148delC:p.Thr383Ilefs*	4	84.86	ND	50
BPE-012	F	6	OD	c.1148delC:p.Thr383Ilefs*	1	82.37	ND	35
BPE-018	M	8	OD	c.1148delC:p.Thr383Ilefs; c.819_826del8:p.Arg274Valfs	1	79.87	53,554	44
BPE-019	F	23	OS	c.1148delC:p.Thr383Ilefs; c.1751T>C:p.Leu584Pro†	4	59.90	11,240	43
BPE-022‖	M	31	OD	c.1148delC:p.Thr383Ilefs*	4	67.39	ND	35
CEI-001‖	M	18	OD	c.1148delC:p.Thr383Ilefs*	2	61.15	13,554	44
CEI-002	M	33	OD	c.1148delC:p.Thr383Ilefs; c.819_826del8:p.Arg274Valfs	2	47.42	21,157	46
CEI-003	F	9	OD	c.1148delC:p.Thr383Ilefs*	1	73.63	ND	34
CEI-004	M	11	OD	c.1148delC:p.Thr383Ilefs; c.886_896del11insT:p.Arg296Tyrfs	2	122.30	ND	63
CEI-005	M	13	OD	c.1148delC:p.Thr383Ilefs*	1	74.88	ND	37
CEI-006	M	31	OD	c.1148delC:p.Thr383Ilefs*	1	68.64	42,314	44
CEI-008	F	16	OD	c.1148delC:p.Thr383Ilefs*	1 (2)	81.12	27,107	44
CEI-009	F	30	OS	c.1148delC:p.Thr383Ilefs*	4	72.38	13,884	38
CEI-010	F	16	OD	c.1148delC:p.Thr383Ilefs; c.1306A>C:p.Ser436Arg	1	73.63	ND	32
CEI-011	M	22	OD	c.1148delC:p.Thr383Ilefs*	1	96.10	ND§	44
CEI-015	M	8	OD	c.1148delC:p.Thr383Ilefs*	1	112.32	ND	37
CEI-016	M	16	OD	c.1148delC:p.Thr383Ilefs*	1	69.89	ND	27
PCI-001	M	26	OD	c.1148delC:p.Thr383Ilefs*	1	99.84	35,702	40
PCI-002	M	18	OD	c.1148delC:p.Thr383Ilefs*	1	84.86	ND	42
PCI-003	M	55	OD	c.1148delC:p.Thr383Ilefs*	5	0	0	45
PCI-004	F	13	OD	c.1148delC:p.Thr383Ilefs*	2	66.14	15,868	48
PCI-005	F	11	OD	c.1148delC:p.Thr383Ilefs*	2 (1)	54.91	ND	40
PCI-006	F	10	OD	c.1148delC:p.Thr383Ilefs; c.503C>T:p.Thr168Met; c.1602T>G:p.Tyr534Ter#	4	68.64	10,579	36
PCI-007	M	17	OD	c.1148delC:p.Thr383Ilefs*	2	84.86	12,231	46
PCI-008‖	F	40	OD	c.1148delC:p.Thr383Ilefs*	4	51.17	7,273	29
PCI-009	M	17	OD	c.1148delC:p.Thr383Ilefs*	2	58.66	19,835	42
PCI-010	M	23	OD	c.1148delC:p.Thr383Ilefs; c.1006G>T:p.Glu336Ter	5	0	0	50
PCI-011	F	44	OD	c.1148delC:p.Thr383Ilefs; c.983T>A:p.Met328Lys†	2	79.87	ND	38
PCI-012‖	F	8	OD	c.1148delC:p.Thr383Ilefs; c.819_826del8:p.Arg274Valfs	4	62.40	ND	36
PCI-013	M	17	OD	c.1148delC:p.Thr383Ilefs; c.819_826del8:p.Arg274Valfs	4	61.15	16,860	46
PCI-017	M	35	OD	c.1148delC:p.Thr383Ilefs*	2	61.15	16,860	50
PCI-019	M	10	OD	c.1148delC:p.Thr383Ilefs; c.1006G>T:p.Glu336Ter	1	59.90	ND	45
PCI-020	M	27	OD	c.819_826del8:p.Arg274Valfs; c.1781+1G>C: splice defect	2	68.64	31,405	45
PCI-021	M	37	OD	c.1148delC:p.Thr383Ilefs; c.983T>A:p.Met328Lys†	2	73.63	44,959	51
PCI-024	F	42	OD	c.1148delC:p.Thr383Ilefs*	1	73.63	ND	37
PCI-025	F	18	OD	c.1148delC:p.Thr383Ilefs; c.1432C>T:p.Arg478Ter	4	54.91	8,926	ND
PCI-031	F	32	OD	c.1148delC:p.Thr383Ilefs*	4	76.13	ND	39
PCI-032	F	28	OS	c.1148delC:p.Thr383Ilefs*	2	82.36	26,777	44
PCI-033	M	32	OS	c.1148delC:p.Thr383Ilefs*	4	69.89	7,603	47
PCI-034	M	43	OD	c.1148delC:p.Thr383Ilefs*	4	81.12	ND	42
UFC-001	M	24	OD	c.1148delC:p.Thr383Ilefs*	4	56.16	12,893	42
UFC-002	F	33	OD	c.1148delC:p.Thr383Ilefs*	4	52.42	16,198	42
UFC-003	F	43	OD	c.1148delC:p.Thr383Ilefs*	2	68.64	22,479	30
UFC-004	F	8	OD	c.1148delC:p.Thr383Ilefs; c.1320+4A>G**	1	64.90	38,678	38

TABLE. Continued

Subject	Sex	Age, y	Eye	Genotype	OCT Grade‡	ONL Thickness, μm	Peak Cone Density, cones/mm^2	Visual Acuity Letter Score
UFC-005	M	14	OD	c.1148delC:p.Thr383Ilefs*	1	89.86	ND	33
UFC-006	M	8	OD	c.1148delC:p.Thr383Ilefs*	3	54.91	17,851	30
UFC-007	F	22	OD	c.1148delC:p.Thr383Ilefs*	4 (2)	93.60	ND	40
UFC-008	M	17	OD	c.1148delC:p.Thr383Ilefs*	1	94.85	ND	40
UFC-009	M	15	OD	c.1148delC:p.Thr383Ilefs*	1	93.60	ND	42
UFC-010	F	38	OD	c.1148delC:p.Thr383Ilefs*	5 (2)	0	0	30

ND, no data; F, female; M, male.

* Subject is homozygous for this mutation.

† To our knowledge this mutation has not been previously reported. The likely pathogenicity was determined using SIFT, PolyPhen-2, and PROVEAN analysis tools. SIFT (version 1.03, in the public domain, http://sift.jcvi.org/, accessed January 2016) results are reported to be tolerated if tolerance index > 0.05 or damaging if tolerance index ≤ 0.05. PolyPhen-2 (version 2.2.2, in the public domain, http://genetics.bwh.harvard.edu/pph2/, accessed January 2016) appraises mutations qualitatively as Benign, Possibly Damaging, or Probably Damaging based on the model's false–positive rate. PROVEAN (version 1.1, in the public domain, http://provean.jcvi.org/human_protein_batch_submit.php, accessed January 2016) results are reported as having a neutral or deleterious effect as determined by averaged delta alignment scores. The p.Leu584Pro mutation was found to be probably damaging, damaging, and deleterious by these tools, respectively, and the p.Met328Lys mutation was found to be benign, damaging, and deleterious.

‡ OCT grade for other eye noted in parentheses if different from that for the eye imaged with AOSLO.

§ The cones in this subject's foveal center were too closely packed to measure with our current split-detector modality. As such, this subject has a higher peak density than all other subjects.

‖ Additional mutations in ACHM-associated genes (see Supplemental Table S1).

¶ These subjects were genetically confirmed at sites other than the Casey Eye Institute Molecular Diagnostic Lab. CEI-015 at University of Colorado, CEI-016 at Children's Hospital of Philadelphia, and PCI-019 at the Wynn Institute for Vision Research Carver Laboratory.

To our knowledge this mutation has not been previously reported; the early termination of this protein is expected to be damaging.

** To our knowledge this mutation has not been previously reported, and is predicted disease causing by MutationTaster.

boundary is the internal limiting membrane (ILM), while in individuals with hypoplasia it is typically the outer plexiform layer (OPL).[36] Additionally, Cirrus HD-OCT (Carl Zeiss Meditec, Dublin, CA, USA) line and volume scans were acquired along with a corresponding line scan ophthalmoscope fundus image to determine the location of the center of the foveal pit.

Adaptive Optics Scanning Light Ophthalmoscopy (AOSLO)

Confocal and split-detector AOSLO images were simultaneously acquired using a previously described instrument.[30,42] Wavefront sensing was performed with an 850 nm superluminescent diode (SLD) and retinal images were acquired using a 790 nm SLD. Image sequences were captured as AVI files using both a 1° × 1° and 1.75° × 1.75° field of view; if eye movement prevented acquisition of nondistorted 1° images only the large field of view was recorded. The images with the smallest field of view (and therefore higher resolution) were used for analysis where possible. The subject was instructed to follow a fixation target to bring different retinal locations into view. The imaging protocol included a 5° × 5° grid centered on the fovea (sampled at 1°-intervals), and 1°-interval sampling out to 12°-eccentricity along the temporal and superior meridians. At each retinal location, two image sequences were simultaneously acquired—one using the confocal channel and one from the split-detection channel.

Sinusoidal distortions are present in the raw images due to the scanning nature of the system, and were corrected by measuring the distortion with a Ronchi ruling of known spacing, and resampling the images. The individual image sequences were then processed as follows. First, a set of reference frames visually judged to have minimal distortion was manually selected from an image sequence (confocal or split-detector), and the remaining frames were broken up into strips and aligned to the reference frame based on normalized cross correlation, as previously described.[43] As the split-detector and the confocal images were simultaneously

acquired at each location, the registration transformations for one modality were applied to the image sequence obtained with the other modality at that same retinal location. The registered image sequences were then averaged to improve the signal-to-noise ratio, and this process resulted in a single confocal TIFF image and a single split-detection TIFF image for each reference frame chosen within a given image sequence.

The TIFF images were then imported into Photoshop (Adobe Photoshop; Adobe Systems, Inc., San Jose, CA, USA) using custom software in MATLAB (Mathworks, Natick, MA, USA) that allows the user to choose the best quality registered images from each retinal location and automatically imports them into a Photoshop document while adjusting the image scale. They were then manually stitched together into a two-layered montage of the split detector and confocal images. Registered TIFF images from both modes generated from a given reference frame were imported together and their position linked to one another—ensuring that any movement of the frame from one mode would also move the other type of image. A color-merged image was also produced by combining these modalities for easier visualization of the regions with absent confocal signal and cone structure observable with split-detector imaging. The image scale was calculated by first determining the degrees per pixel in an image of a ruling with known spacing using the small angle approximation. This value was then linearly scaled using the subject's axial length and a reference axial length of 24 mm, and multiplied by the retinal magnification factor of 291 μm/degree to obtain a final micrometer per pixel scale. The final montage was aligned with the Cirrus SLO image using Photoshop, which had the foveal center marked to allow for identification of the foveal pit center on the AOSLO images, to confirm that the region analyzed was the rod-free zone at the fovea.

Measuring Foveal Cone Density

For each subject, the eye with better image quality and less motion artifact was chosen for quantitative analysis. Confocal
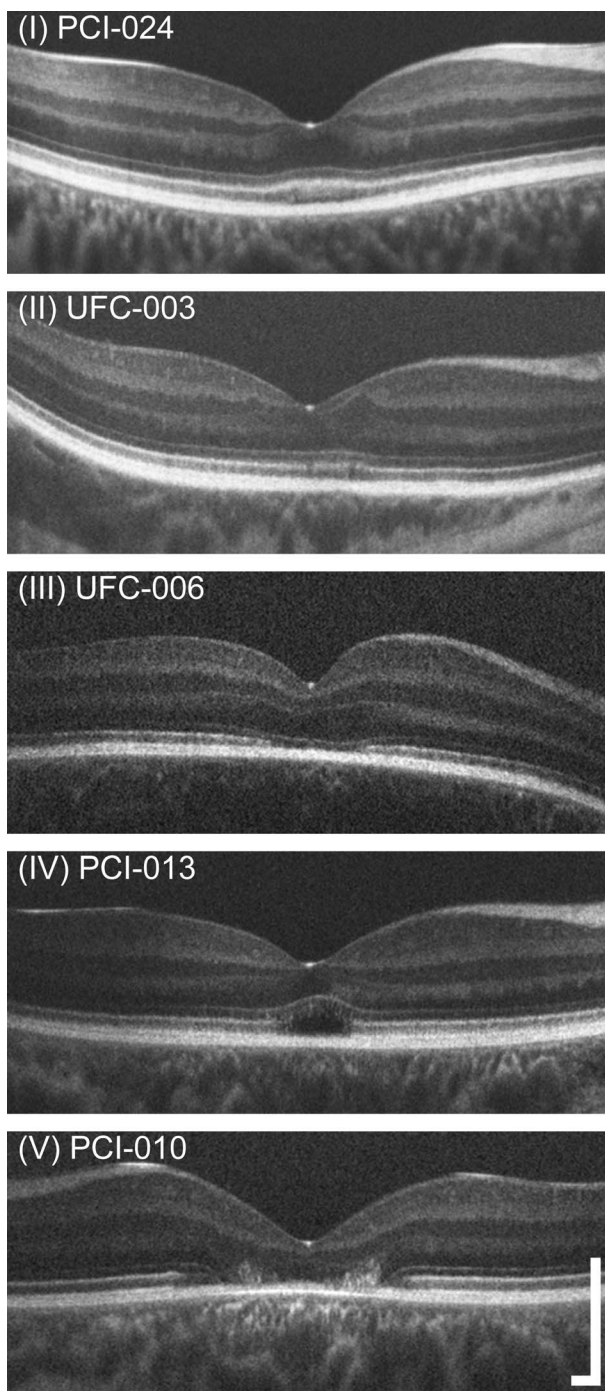
FIGURE 1. Examples of the grades used for OCT phenotyping. The scheme used here is based on that of Sundaram et al.,[26] who based their grading on the appearance of the EZ band (also, IS/OS junction). Grade I corresponds to a continuous band, Grade II corresponds to a disrupted band, Grade III corresponds to an absence or collapse of the band, and Grade IV corresponds to the presence of a hyporeflective zone (HRZ). Subjects with outer retinal atrophy were labeled as Grade V. These OCTs are displayed a logarithmically transformed intensity scale. The distribution of grades present in our subjects is given in the Table. *Scale bar*: 250 μm.

FIGURE 2. Longitudinal reflectivity profiles from log transformed OCT images of retinas without (**A**) and with (**B**) foveal hypoplasia. In both cases, the longitudinal reflectivity profile was averaged over a 5-pixel wide region positioned at the center of the foveal depression. (**A**) In a subject with normal foveal excavation, the ONL is bounded by hyperreflective peaks corresponding to the ILM and the ELM. (**B**) In this subject with foveal hypoplasia, the ONL is bounded by hyper-reflective peaks corresponding to the OPL and the ELM. For all subjects, the distance between the ELM and the OPL was taken as the foveal ONL thickness.[26,38] Of our 52 subjects, 37 (71%) had some degree of foveal hypoplasia.

and split-detector montages were used to define the approximate extent of the rod-free zone at the fovea (Supplementary Fig. S1). The exact rod-free zone was not necessary to outline, so long as the region of highest cone density was captured within this area. All cones observed with the split-detector mode were manually marked within the rod-free zone to generate an array of cone coordinates. To assess peak foveal density, a 55×55 μm sampling window was used to determine density in cones per square millimeter at each pixel within the coordinate array. The pixel location with the greatest value was taken to be the location of peak foveal density. Cone density was then compared with the grade of the EZ disruption as well as the ONL thickness on OCT.

RESULTS

Demographics and Genetics

Twenty-one female and 30 male subjects were recruited with a mean age of 22.8 years (range, 6–55 years). Mean (±SD) axial length was 24.26 ± 1.87 mm (range, 19.8–28.31 mm). All subjects had at least two mutations in the *CNGB3* gene, with 35 (69%) being homozygous and 14 (27%) being heterozygous for the c.1148delC mutation (Table). Four previously unre-

ported mutations were identified: c.1751T>C:p.Leu584Pro, c.983T>A:p.Met328Lys, c.1602T>G:p.Tyr534Ter, and c.1320+4A>G, all of which were considered to be disease-causing (Table). Additionally, five subjects harbored mutations in other ACHM-associated genes (Supplementary Table S1). Visual acuity (ETDRS) ranged from 8 to 63 letters.

Optical Coherence Tomography Demonstrates Variability in Foveal Structure

Significant variation in outer retinal structure was seen on OCT. Foveal hypoplasia (retained inner retinal layers at the foveal center) was observed in 37 subjects (71%), consistent with the frequency reported in previous studies.[23,26] With regards to the appearance of the second hyperreflective band (EZ or IS/OS), 18 subjects had a grade I phenotype, 13 were grade II, 1 was grade III, 16 were grade IV, and 3 were grade V (Table). This result does not differ significantly from the distribution of OCT grades in *CNGB3*-associated ACHM reported by Sundaram et al.[26] ($P = 0.319$, Fisher's exact test). The presence of foveal hypoplasia did not correlate with OCT grade ($P = 0.5208$, Wilcoxon Mann-Whitney test).

Outer nuclear layer thickness ranged from 0 to 122 μm; mean ± SD ONL thickness for the grade I retinas was 81.9 ± 13.7 μm, 71.5 ± 18.8 μm for the grade II retinas, 71.5 μm for the grade III retina, and 68.7 ± 13.0 μm for the grade IV retinas (Table). As OCT grade V was always associated with an ONL thickness value of 0 μm (there is no outer retina present in these atrophic cases) these values were excluded from statistical analysis of ONL thickness. Compared with previously published normal values (mean ± SD = 105 ± 12.2 μm, $n = 93$, mean age ± SD = 29 ± 8.42),[44] the ACHM subjects had a significantly thinner ONL (mean ± SD = 74.1 μm ± 16.0 μm, $n = 48$; $P < 0.0001$, t-test). The presence of foveal hypoplasia did not correlate with ONL thickness ($P = 0.1902$, Wilcoxon Mann-Whitney test).

Variability in Remnant Foveal Cone Density

Low image quality as a result of nystagmus, poor fixation, and other factors precluded acquisition of analyzable images in a portion of the subjects in this study. Despite this limitation, at least some cone structure was observed in raw images of all retinas, though not necessarily at the fovea. The three grade V retinas had no detectable cone structure in the atrophic fovea, but remnant cone IS could be seen in areas immediately adjacent to the atrophic lesion (Supplementary Fig. S2).

We were able to acquire analyzable foveal cone images using split-detector AOSLO in 26 of the remaining 48 subjects (54%). The presence of foveal hypoplasia did not correlate with our ability to acquire analyzable AOSLO images ($P = 1.00$, Fisher's Exact test). Peak cone density ranged from 7,273 to 53,554 cones/mm^2, with a mean value of 21,373 cones/mm^2 for this cohort (Table). While there is great variation in the peak density among these subjects, the values shown here are significantly below, and do not overlap with, previously published normative values (range, 84,733–247,061 cones/mm^2).[45,46] The presence of foveal hypoplasia did not correlate with peak cone density ($P = 0.4943$, Wilcoxon Mann-Whitney test). The location of peak density was not found to be near the border of the examined region in any case.

In addition to variability in peak density, there was variability of the appearance of the residual foveal cone population from a contiguous mosaic to a sparse collection of cells (Fig. 3). We quantified this by determining the inter-cell distance (ICD) for each cell in the rod-free zone, which is the distance between each cell and its immediate neighbors. We

then calculated the mean (μ) and SD (σ) of the ICD for each subject in order to find the coefficient of variation (CV = σ/μ), which indicates the overall variability in ICD independent of the actual ICD values (which vary widely across subjects). We determined what the range of the CV value was for our subjects, and six nondiseased retinas. There was generally greater variation in the ICD in the ACHM subjects (CV mean ± SD = 0.261 ± 0.066), than the healthy subjects (CV mean ± SD = 0.130 ± 0.014; $P < 0.001$, t-test; Fig. 4). The ICD values were higher in the ACHM group (mean ± SD = 12.59 ± 4.37 μm) than the nondiseased group (mean ± SD = 3.61 μm ± 0.22 μm; $P < 0.001$, t-test). The difference in ICD and CV indicate that the ACHM mosaics were less evenly spaced and generally more sparsely distributed than normal retinas. In addition, the reflectivity of these remnant cones on confocal AOSLO was abnormal, with only a few cones showing a central reflective core on confocal AOSLO imagery. This is consistent with previous reports in which 1% of cones in subjects with *CNGB3*-associated ACHM were reported to have normal reflectivity on confocal AOSLO.[25]

Comparing AOSLO and OCT Measures of Cone Structure

As the different measures of cone structure presented here likely reflect different aspects of cone anatomy, it is important to examine the relationship between these two measures to provide a better understanding of cone health in the ACHM retina. Measurements from the grade III retina were removed from analyses involving OCT grade due to the sample size restriction, while grade V retinas were excluded from analyses involving peak cone density or ONL thickness. We first examine the relationship between OCT grade and peak cone density and ONL thickness (Fig. 5). Using the Kruskal-Wallis test, we observed a significant association between OCT grade and both peak cone density ($P = 0.0003$) and ONL thickness ($P = 0.0176$). Further pairwise comparisons revealed significant differences between OCT grades I & II and grades I & IV for both peak cone density ($P = 0.0143$ and $P = 0.0022$) and ONL thickness ($P = 0.0289$ and $P = 0.0096$). Whether the reduced ONL thickness in the grade IV retinas is due to the protrusion of the hyporeflective zone pushing the ELM inward or actual loss of cone nuclei is not clear. We observed no correlation between foveal ONL thickness and peak cone density ($P = 0.1462$, Spearman Correlation). This latter finding may not be surprising, as the relationship between ONL measurements and cone IS is likely to be complex. First, our ONL measures are likely contaminated (albeit to a small degree) by residual Henle fiber layer that is not easily differentiated from "true" ONL without performing directional OCT.[47,48] Moreover, it is not possible to determine the contribution of rod nuclei to our "foveal" ONL measurements.

Effect of Age on Measures of Cone Structure

Given the debate surrounding the progressive nature of ACHM, and the impact of this on defining potential therapeutic windows, we examined whether any of the anatomic measures reported here showed an association with age. As shown in Figure 6A, a significant association was observed between age and the different OCT grades ($P = 0.0099$, Kruskal-Wallis test), with II, IV, and V being different from grade I ($P = 0.018$, 0.0155, and 0.0205, respectively, Kruskal-Wallis test). There was no relationship between age and ONL thickness ($P = 0.2988$, Spearman correlation) or age and peak-cone density observed ($P = 0.9796$, Spearman correlation; Figs. 6B, 6C).
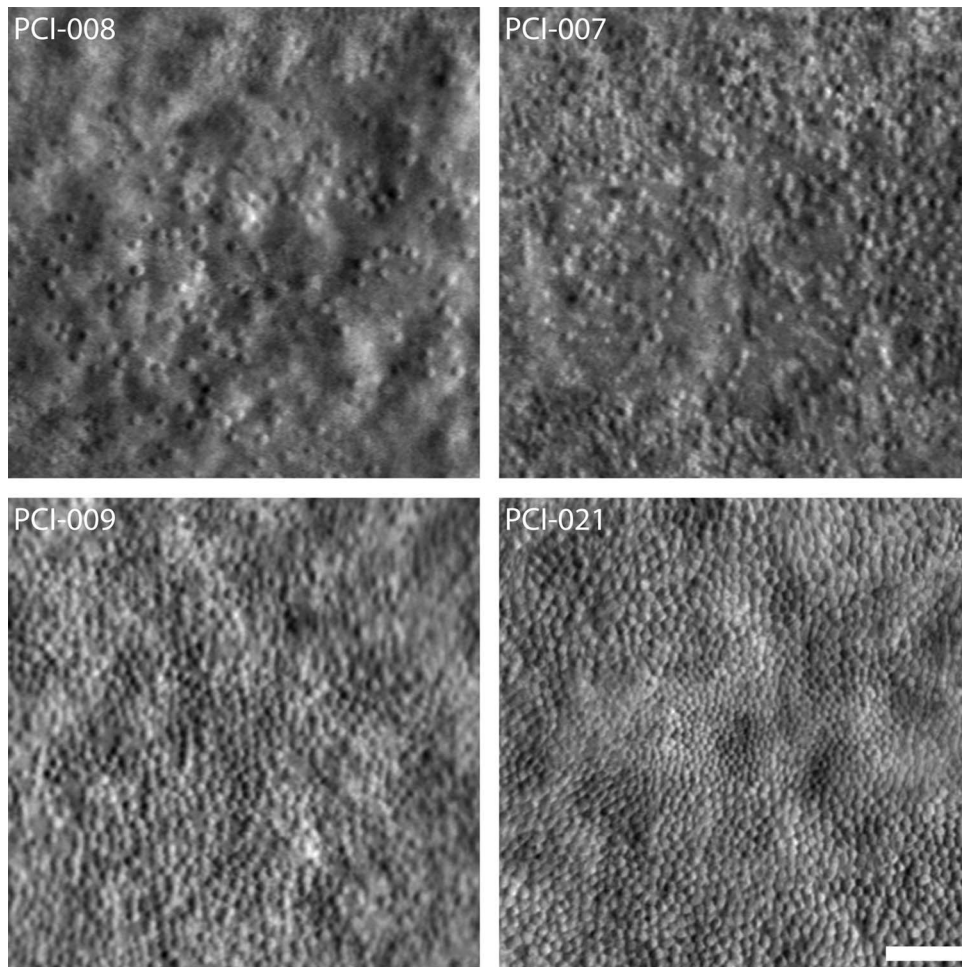
FIGURE 3. Variability in the foveal cone mosaic in patients with ACHM. (*Top*) Foveal montages obtained using split-detector AOSLO for two subjects with sparse foveal mosaics—PCI-008 with a peak density of 7,273 cones/mm² and PCI-007 with 12,231 cones/mm². (*Bottom*) Foveal montages for two subjects with relatively contiguous mosaics—PCI-009 with a peak density of 19,835 cones/mm² and PCI-021 with 44,959 cones/mm². *Scale bar*: 50 μm.
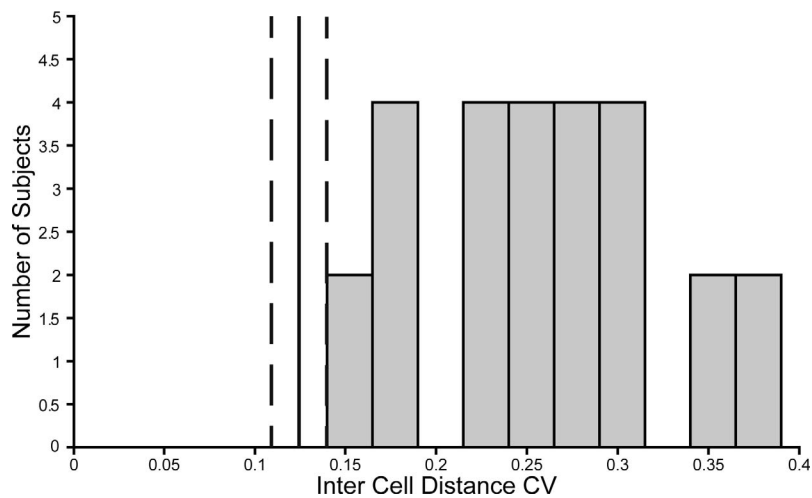

FIGURE 4. Variability in inter-cell distance (ICD). Measurements of ICD from all subjects were made and the CV was calculated for each subject. Shown is a histogram of the distribution of the CV for all ACHM subjects with quantified foveal cone populations. The *vertical solid line* denotes the mean and *dashed lines* the range of the normal CV from measurements made on the foveal cone populations of six nondiseased retinas.
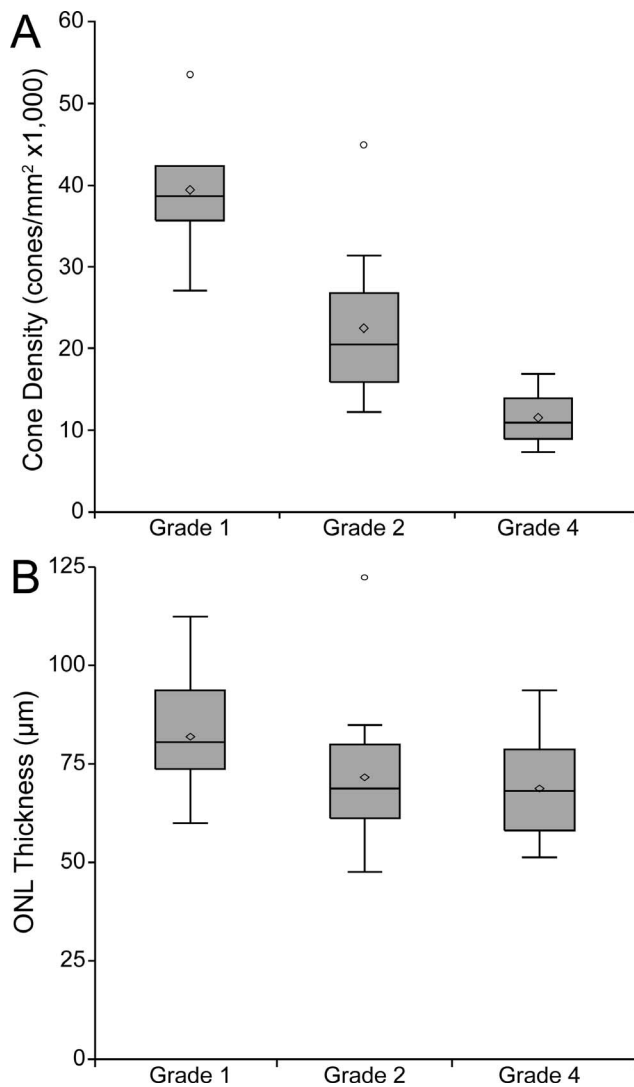
Figure 5. Comparison of cone structure determined by OCT and AOLSO. Comparing OCT grade versus peak cone density (**A**) shows a significant difference among grades I, II, and IV ($P = 0.0003$), though there remains significant overlap in the ranges of these grades. Comparing ONL thickness to OCT Grade (**B**) revealed a relationship between these measurements ($P = 0.0176$). *Shaded regions* represent the first through third quartile, the *horizontal line* the median, the *extending lines* represent the maximum and minimum, the *diamond* the mean, and *circles* signify outliers.

DISCUSSION

We observed remnant cone IS structure in all subjects in this study. Of subjects with analyzable foveal cone images, the number and spatial distribution of the foveal cones were highly variable—the foveal cone mosaic ranged from a contiguously packed mosaic to a sparsely arranged collection of cones. Of the 48 subjects with grades I to IV retinas, only 26 had images of sufficient quality to be processed, montaged, and quantified. Nystagmus and/or unstable fixation were the primary reasons for our inability to process the remaining subjects, though there may be future opportunities to improve the ability of AOSLO devices to image these challenging patients by implementing eye-tracking tools. Despite this current limitation, it should be noted that even in individual raw AOSLO frames, there was clear evidence of remnant cone structure in these subjects (Supplementary Fig. S3), including those with

grade V retinas (Supplementary Fig. S2), though it was not possible to quantify cone density in these cases. Our finding of remnant cone IS structure in all *CNGB3* ACHM retinas is supported by some older histologic reports,[49,50] though these were published prior to the era of molecular genetic diagnostic capabilities.

The remnant cones visualized with split-detector AOSLO had low reflectivity in the corresponding confocal AOSLO images, consistent with previous reports in patients with ACHM,[20,21,23,25,30] some red-green color vision defects,[44,51,52] and blue-cone monochromacy.[44,53] Split-detector imaging, however, can reveal cone IS even when those cones are lacking the necessary waveguide properties for visualization with confocal AOSLO and AO funduscopy.[30] Rods retain their reflectivity in ACHM, and surround the nonreflective "dark" cones in confocal AOSLO images acquired outside the fovea, allowing for fairly reliable identification of the remnant dark cones. However, this method of determining cone locations breaks down in areas with no rod structure (e.g., the fovea), where it becomes necessary to use split-detector imaging to reliably identify the cones. This technique has been used to identify cones in other disorders where they have altered reflectivity.[32,33] As the confocal and split-detector images are acquired simultaneously and are spatially coregistered, they can be used to differentiate between cones passing higher order waveguide modes, rods, and nonphotoreceptor structures like RPE. It is important to note that we view these AOSLO techniques as complementary to one another and are not proposing that one is superior to the other, rather that both will play an important role in evaluating cone structure in inherited retinal degenerations.

One limitation of the present study is that we did not relate functional measures to any of the structural measures—this was intentional. One reason for this is the prevalence of nystagmus in this population—this makes it difficult to make accurate measurements of acuity and can confound ERG measurements. Moreover, with only a few exceptions, the acuity measures in our subjects are quite homogenous (Table). In order to make meaningful correlations between various modalities, it is necessary to have a reasonable spread of values with which to infer structure/function relationships. Additionally, functional measures like the ERG are a diffuse measure of visual function, while the structural measures made here are focal in nature. That said, the fact that patients have residual cone structure (presence of ONL and remnant cone IS) provides an anatomic basis for the residual 30-Hz flicker response on ERG observed previously in patients with ACHM,[54] though the widespread retention of cone function on ERG has not been confirmed by others.[16,55] In addition, it would be interesting to determine whether individuals with greater numbers of foveal cones (either IS remnants of ONL thickness) showed the same degree of cortical reorganization as has been reported in some ACHM patients,[56] as this is a potential complication in the pursuit of restoring cone vision in patients with ACHM.

This study examined correlations between OCT imaging and cellular level AOSLO imaging. While ONL thickness does not correlate with peak cone density, less severe EZ phenotypes were associated with higher peak density values. This result does not, however, mean that the OCT grade can be used as a surrogate for cone density, given the wide overlapping range of cone densities within the grades I and II groups. While the highest cone density was seen in grade I or II retinas, there were also subjects with these less disrupted grade I and II OCT phenotypes whose density fell within the range observed for the grade III and IV retinas. This result indicates that a more severe OCT phenotype may be evidence for a low cone density, but a less disrupted OCT grade could
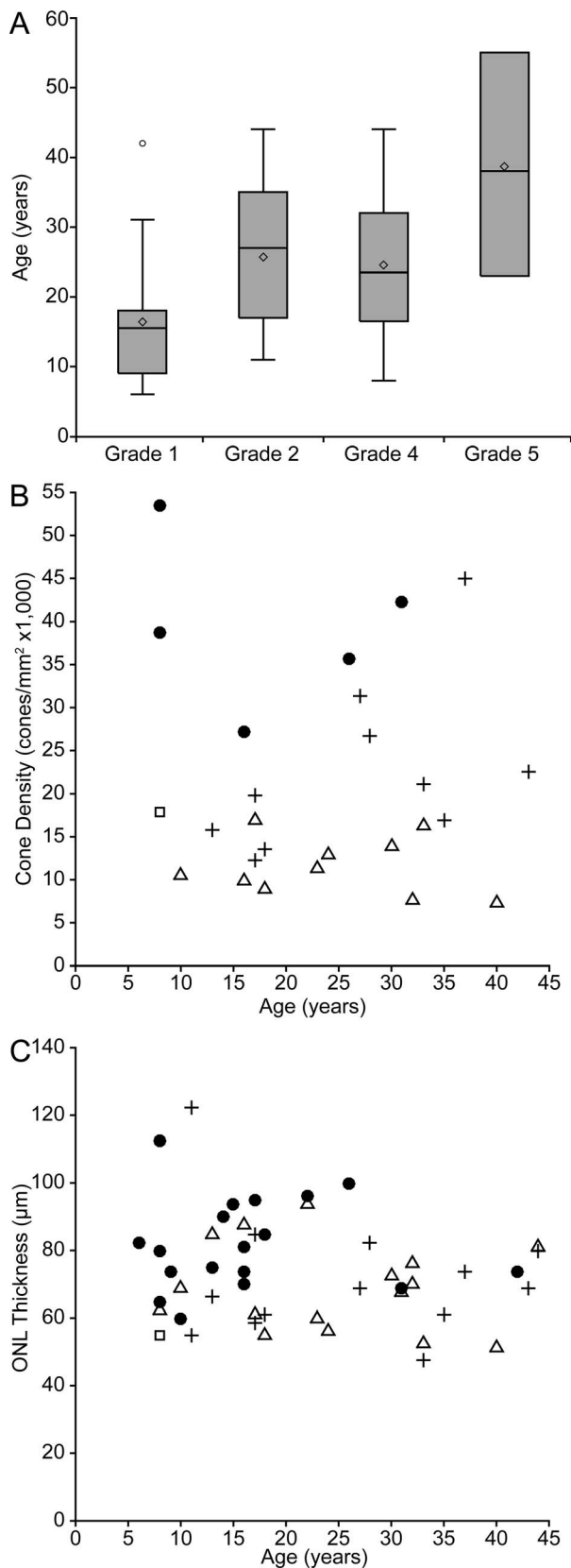
FIGURE 6. Cone structure measurements compared with age. In (**A**) OCT grade was found to have an age relationship ($P = 0.0099$), with more severe OCT grades being found in older individuals on average. *Shaded regions* represent the first through third quartile, the *horizontal line* the median, the *extending lines* represent the maximum and minimum, the *diamond* the mean, and *circles* signify outliers. In contrast, neither ONL thickness (**B**) nor peak cone density (**C**) showed an age relationship. Symbols in (**B**) and (**C**) represent the OCT grade: *filled circles*, grade I; *crosses*, grade II; *squares*, grade III; *triangles*, grade IV.

correspond to either a high or low cone density. The presence of remnant IS cone structure in all grades I to IV retinas indicates that disruptions in the EZ band on OCT do not necessarily correlate to the degree of photoreceptor loss measured with AOSLO in that region.[32] Of course there is a concrete relationship in the grade V retinas, where there is a complete absence of cones within the atrophic region. It will be interesting to monitor how these various relationships between AOSLO- and OCT-derived measures of cone structure (cone density and ONL thickness, respectively) change over time, as we would predict small changes in foveal cones to manifest on AOSLO before OCT. The variability in this population points toward a need for longitudinal analysis of individuals to determine if there is progressive loss of cone structure within this or other genotypes. We should note that while our cross-sectional data suggest no association between cone density and age, previous studies have reported reduced parafoveal cone density in normal aging[57,58]; thus, it will be important to factor this into any subsequent longitudinal studies of parafoveal cone structure.

The present study focused entirely on *CNGB3*-associated ACHM, motivated by an upcoming gene therapy trial targeting patients with *CNGB3* mutations (in the public domain, www.clinicaltrials.gov, NCT02599922). There is evidence for genotype-dependent differences in visual function in patients with ACHM. For example, patients with ACHM caused by *GNAT2* mutations have been shown to have some cone-mediated response to low-frequency stimuli.[59] It was recently shown that these patients also have different photoreceptor structure than their *CNGA3* or *CNGB3* counterparts, with significantly greater numbers of cones exhibiting normal waveguiding behavior.[25] As there is at least one trial enrolling patients with *CNGA3*-associated ACHM (in the public domain, www.clinicaltrials.gov, NCT02610582), it will be important to establish the degree of residual cone structure in these individuals as well, as the cone population (the target of gene therapy) may vary between genotypes. Retinas with larger numbers of cone IS may have a greater therapeutic potential than individuals with fewer remnant cones. In addition, the viability of remnant cone soma (that may not have a detectable IS) needs to be considered (i.e., it may be that the split-detector provides an underestimate of residual cone structure, though our inability to image cone soma makes this a difficult hypothesis to test). Moving forward, it will be important to consider how (or if) to use this anatomic information when considering patients for enrollment. For example, consider a trial participant who shows no response to a given intervention; in the absence of accurate baseline information on residual cone structure, it would be difficult to determine if the lack of response is due to an ineffective treatment or whether there were simply too few cones (even if those cones became fully functional) to drive a change in visual behavior.[60] Furthermore, the reflectivity of cone cells may recover as normal structure (and therefore normal waveguiding) is restored in them with therapy. This may provide a means of monitoring OS revival in treated cones.

In conclusion, split-detection AOSLO imaging appears to hold significant potential as a tool for probing residual cone structure in retinas disrupted by diseases like ACHM. Moving

forward, AOSLO will be useful for continuing to understand the photoreceptor structure in multiple diseases and how structure may differ between genotypes within a given disorder. Additionally, cellular resolution imaging will be an important tool for planning and carrying out future trials to aid in patient selection, monitoring structure throughout the trial, and correlating cone structure to trial outcomes.

References

1. Michaelides M, Hunt DM, Moore AT. The cone dysfunction syndromes. *Br J Ophthalmol*. 2004;88:291–297.

2. Sharpe LT, Stockman A, Jägle H, Nathans J. Opsin genes, cone photopigments, color vision, and color blindness. In: Gegenfurtner KR, Sharpe LT, eds. *Color Vision: From Genes to Perception*. New York, NY: Cambridge University Press; 1999: 3–52.

3. Zobor D, Zobor G, Kohl S. Achromatopsia: on the doorstep of a possible therapy. *Ophthalmic Res*. 2015;54:103–108.

4. Thiadens AA, Somervuo V, van den Born LI, et al. Progressive loss of cones in achromatopsia: an imaging study using spectral-domain optical coherence tomography. *Invest Ophthalmol Vis Sci*. 2010;51:5952–5957.

5. Thomas MG, McLean RJ, Kohl S, Sheth V, Gottlob I. Early signs of longitudinal progressive cone photoreceptor degeneration in achromatopsia. *Br J Ophthalmol*. 2012;96:1232–1236.

6. Kohl S, Marx T, Giddings I, et al. Total colour blindness is caused by mutations in the gene encoding the alpha-subunit of the cone photoreceptor cGMP-gated cation channel. *Nat Genet*. 1998;19:257–259.

7. Kohl S, Baumann B, Rosenberg T, et al. Mutations in the cone photoreceptor G-protein α-subunit gene *GNAT2* in patients with achromatopsia. *Am J Hum Genet*. 2002;71:422–425.

8. Kohl S, Varsanyi B, Antunes GA, et al. *CNGB3* mutations account for 50% of all cases with autosomal recessive achromatopsia. *Eur J Hum Genet*. 2005;13:302–308.

9. Thiadens AA, Slingerland NW, Roosing S, et al. Genetic etiology and clinical consequences of complete and incomplete achromatopsia. *Ophthalmology*. 2009;116:1984–1989.

10. Carvalho LS, Xu J, Pearson R, et al. Long-term and age-dependent restoration of visual function in a mouse model of *CNGB3*-associated achromatopsia following gene therapy. *Hum Mol Genet*. 2011;20:3161–3175.

11. Komáromy A, Alexander JJ, Rowlan JS, et al. Gene therapy rescues cone function in congenital achromatopsia. *Hum Mol Genet*. 2010;19:2581–2593.

12. Pang JJ, Deng WT, Dai X, et al. AAV-mediated cone rescue in a naturally occurring mouse model of *CNGA3*-achromatopsia. *PLoS One*. 2012;7:e35250.

13. Du W, Tao Y, Deng W, et al. Vitreal delivery of AAV vectored Cnga3 restores cone function in *CNGA3$^{-/-}$/Nrl$^{-/-}$* mice, an all-cone model of *CNGA3* achromatopsia. *Hum Mol Genet*. 2015; 24:3699–3707.

14. Ezra-Elia R, Banin E, Honig H, et al. Flicker cone function in normal and day blind sheep: a large animal model for human achromatopsia caused by *CNGA3* mutation. *Doc Ophthalmol*. 2014;129:141–150.

15. Banin E, Gootwine E, Obolensky A, et al. Gene augmentation therapy restores retinal function and visual behavior in a sheep model of *CNGA3* achromatopsia. *Mol Ther*. 2015;23: 1423–1433.

16. Zelinger L, Cideciyan AV, Kohl S, et al. Genetics and disease expression in the *CNGA3* form of achromatopsia: steps on the path to gene therapy. *Ophthalmology*. 2015;122:997–1007.

17. Jacobson SG, Aleman TS, Cideciyan AV, et al. Identifying photoreceptors in blind eyes caused by *RPE65* mutations: prerequisite for human gene therapy success. *Proc Natl Acad Sci U S A*. 2005;102:6177–6182.

18. Spaide RF, Curcio CA. Anatomical correlates to the bands seen in the outer retina by optical coherence tomography: literature review and model. *Retina*. 2011;31:1609–1619.

19. Jonnal RS, Kocaoglu OP, Zawadzki RJ, Lee SH, Werner JS, Miller DT. The cellular origins of the outer retinal bands in optical coherence tomography images. *Invest Ophthalmol Vis Sci*. 2014;55:7904–7918.

20. Carroll J, Choi SS, Williams DR. In vivo imaging of the photoreceptor mosaic of a rod monochromat. *Vision Res*. 2008;48:2564–2568.

21. Merino D, Duncan JL, Tiruveedhula P, Roorda A. Observation of cone and rod photoreceptors in normal subjects and patients using a new generation adaptive optics scanning laser ophthalmoscope. *Biomed Opt Express*. 2011;2:2189–2201.

22. Hood DC, Zhang X, Ramachandran R, et al. The inner segment/outer segment border seen on optical coherence tomography is less intense in patients with diminished cone function. *Invest Ophthalmol Vis Sci*. 2011;52:9703–9709.

23. Genead MA, Fishman GA, Rha J, et al. Photoreceptor structure and function in patients with congenital achromatopsia. *Invest Ophthalmol Vis Sci*. 2011;52:7298–7308.

24. Aboshiha J, Dubis AM, Cowing J, et al. A prospective longitudinal study of retinal structure and function in achromatopsia. *Invest Ophthalmol Vis Sci*. 2014;55:5733–5743.

25. Dubis AM, Cooper RF, Aboshiha J, et al. Genotype-dependent variability in residual cone structure in achromatopsia: towards developing metrics for assessing cone health. *Invest Ophthalmol Vis Sci*. 2014;55:7303–7311.

26. Sundaram V, Wilde C, Aboshiha J, et al. Retinal structure and function in achromatopsia: implications for gene therapy. *Ophthalmology.* 2014;121:234–245.

27. Roorda A, Romero-Borja F, Donnelly WJ III, Queener H, Hebert T, Campbell M. Adaptive optics scanning laser ophthalmoscopy. *Opt Express.* 2002;10:405–412.

28. Dubra A, Sulai Y, Norris JL, et al. Noninvasive imaging of the human rod photoreceptor mosaic using a confocal adaptive optics scanning ophthalmoscope. *Biomed Opt Express.* 2011; 2:1864–1876.

29. Rossi EA, Chung M, Dubra A, Hunter JJ, Merigan WH, Williams DR. Imaging retinal mosaics in the living eye. *Eye.* 2011;25: 301–308.

30. Scoles D, Sulai YN, Langlo CS, et al. In vivo imaging of human cone photoreceptor inner segments. *Invest Ophthalmol Vis Sci.* 2014;55:4244–4251.

31. Horton JC, Parker AB, Botelho JV, Duncan JL. Spontaneous regeneration of human photoreceptor outer segments. *Sci Rep.* 2015;5:12364.

32. Sun LW, Johnson RD, Langlo CS, et al. Assessing photoreceptor structure in retinitis pigmentosa and Usher syndrome. *Invest Ophthalmol Vis Sci.* 2016;57:2428–2442.

33. Scoles D, Flatter JA, Cooper RF, et al. Assessing photoreceptor structure associated with ellipsoid zone disruptions visualized with optical coherence tomography. *Retina.* 2016;36:91–103.

34. Tanna H, Dubis AM, Ayub N, et al. Retinal imaging using commercial broadband optical coherence tomography. *Br J Ophthalmol.* 2010;94:372–376.

35. Schneider CA, Rasband WS, Eliceiri KW. NIH Image to ImageJ: 25 years of image analysis. *Nat Methods.* 2012;9:671–675.

36. Staurenghi G, Sadda S, Chakravarthy U, Spaide RF, International Nomenclature for Optical Coherence Tomography (IN•OCT) Panel. Proposed lexicon for anatomic landmarks in normal posterior segment spectral-domain optical coherence tomography: The IN•OCT consensus. *Ophthalmology.* 2014; 121:1572–1578.

37. Thomas MG, Kumar A, Mohammad S, et al. Structural grading of foveal hypoplasia using spectral-domain optical coherence tomography a predictor of visual acuity? *Ophthalmology.* 2011;118:1653–1660.

38. Thomas MG, Kumar A, Kohl S, Proudlock FA, Gottlob I. High-resolution in vivo imaging in achromatopsia. *Ophthalmology.* 2011;118:882–887.

39. Hammer DX, Iftimia NV, Ferguson RD, et al. Foveal fine structure in retinopathy of prematurity: an adaptive optics Fourier domain optical coherence tomography study. *Invest Ophthalmol Vis Sci.* 2008;49:2061–2070.

40. Curcio CA, Messinger JD, Sloan KR, Mitra A, McGwin G, Spaide RF. Human chorioretinal layer thicknesses measured in macula-wide, high-resolution histologic sections. *Invest Ophthalmol Vis Sci.* 2011;52:3943–3954.

41. Dubis AM, Costakos DM, Subramaniam CD, et al. Evaluation of normal human foveal development using optical coherence tomography and histologic examination. *Arch Ophthalmol.* 2012;130:1291–1300.

42. Dubra A, Sulai Y. Reflective afocal broadband adaptive optics scanning ophthalmoscope. *Biomed Opt Express.* 2011;2: 1757–1768.

43. Dubra A, Harvey Z. Registration of 2D images from fast scanning ophthalmic instruments. In: Fischer B, Dawant B, Lorenz C, eds. *Biomed Image Registration.* Berlin, Germany: Springer-Verlag; 2010;60–71.

44. Carroll J, Dubra A, Gardner JC, et al. The effect of cone opsin mutations on retinal structure and the integrity of the photoreceptor mosaic. *Invest Ophthalmol Vis Sci.* 2012;53: 8006–8015.

45. Wilk MA, McAllister JT, Cooper RF, et al. Relationship between foveal cone specialization and pit morphology in albinism. *Invest Ophthalmol Vis Sci.* 2014;55:4186–4198.

46. Zhang T, Godara P, Blancob ER, et al. Variability in human cone topography assessed by adaptive optics scanning laser ophthalmoscopy. *Am J Ophthalmol.* 2015;160:290–300.

47. Lujan BJ, Roorda A, Knighton RW, Carroll J. Revealing Henle's fiber layer using spectral domain optical coherence tomography. *Invest Ophthalmol Vis Sci.* 2011;52:1486–1492.

48. Lujan BJ, Roorda A, Croskrey JA, et al. Directional optical coherence tomography provides accurate outer nuclear layer and Henle fiber layer measurements. *Retina.* 2015;35:1511–1520.

49. Falls HF, Wolter JR, Alpern M. Typical total monochromacy. A histological and psychophysical study. *Arch Ophthalmol.* 1965;74:610–616.

50. Harrison R, Hoefnagel D, Hayward JN. Congenital total color blindness: a clincopathological report. *Arch Ophthalmol.* 1960;64:685–692.

51. Carroll J, Baraas RC, Wagner-Schuman M, et al. Cone photoreceptor mosaic disruption associated with Cys203Arg mutation in the M-cone opsin. *Proc Natl Acad Sci U S A.* 2009; 106:20948–20953.

52. Carroll J, Neitz M, Hofer H, Neitz J, Williams DR. Functional photoreceptor loss revealed with adaptive optics: an alternate cause of color blindness. *Proc Natl Acad Sci U S A.* 2004;101: 8461–8466.

53. Cideciyan AV, Hufnagel RB, Carroll J, et al. Human cone visual pigment deletions spare sufficient photoreceptors to warrant gene therapy. *Hum Gene Ther.* 2013;24:993–1006.

54. Nishiguchi KM, Sandberg MA, Gorji N, Berson EL, Dryja TP. Cone cGMP-gated channel mutations and clinical findings in patients with achromatopsia, macular degeneration, and other hereditary cone diseases. *Hum Mutat.* 2005;25:248–258.

55. Khan NW, Wissinger B, Kohl S, Sieving P. *CNGB3* achromatopsia with progressive loss of residual cone function and impaired rod-mediated function. *Invest Ophthalmol Vis Sci.* 2007;48:3864–3871.

56. Baseler HA, Brewer AA, Sharpe LT, Morland AB, Jägle H, Wandell BA. Reorganization of human cortical maps caused by inherited photoreceptor abnormalities. *Nat Neurosci.* 2002;5: 364–370.

57. Song H, Chui TY, Zhong Z, Elsner AE, Burns SA. Variation of cone photoreceptor packing density with retinal eccentricity and age. *Invest Ophthalmol Vis Sci.* 2011;52:7376–7384.

58. Chui TY, Song H, Clark CA, Papay JA, Burns SA, Elsner AE. Cone photoreceptor packing density and the outer nuclear layer thickness in healthy subjects. *Invest Ophthalmol Vis Sci.* 2012;53:3545–3553.

59. Stockman A, Smithson HE, Michaelides M, Moore AT, Webster AR, Sharpe LT. Residual cone vision without α-transducin. *J Vis.* 2007;7(4):8.

60. Langlo C, Dubis A, Michaelides M, Carroll J. Comment on: *CNGB3*-achromatopsia clinical trial with CNTF: diminished rod pathway responses with no evidence of improvement in cone function. *Invest Ophthalmol Vis Sci.* 2015;56:1505.

APPENDIX

The members of the ACHM-001 study group include:

Applied Genetics Technologies Corporation: Jeffrey D. Chulay, June Lato, Rabia Ozden, and John Burnett

Bascom Palmer Eye Institute at University of Miami: Byron L. Lam, Potyra Rosa, and Jennifer Verriotto

Casey Eye Institute at Oregon Health and Science University: Mark E. Pennesi, Paul Yang, Richard G. Weleber, Mihir Wanchoo, and Deanna Ternes

Casey Eye Institute Reading Center: Maria Parker, Laura R. Erker, and David J. Wilson

Casey Eye Institute Molecular Diagnostic Lab: John Chiang

The Chicago Lighthouse: Gerald A. Fishman, Frederick T. Collison, Carol White, and Paola Andreuzzi

Medical College of Wisconsin: Joseph Carroll, Alfredo Dubra, Vesper Williams, Phyllis Summerfelt, Emily J. Patterson, and Christopher S. Langlo

University of Florida: William W. Hauswirth

Vitreoretinal Associates of Gainesville: Christine N. Kay and Jing Zhang